nature communications

Article

https://doi.org/10.1038/s41467-025-65261-6

Unraveling the hydrogen spillover in tandem propane dehydrogenation and reverse water gas shift reaction

Received: 15 April 2025

Accepted: 10 October 2025

Published online: 19 November 2025

Check for updates

Kaige Tian[1,9], Sai Chen[1,2,9], Guodong Sun[1,2,3,4,5,9], Jiachen Sun[1], Xianhui Wang[1,6], Jianhua Cai[1], Zhiyuan Wang[1], Donglong Fu[1,2], Zhi-Jian Zhao[1,2,4,5], Chunlei Pei[1,2,4,5,6] ✉ & Jinlong Gong[1,2,7,8] ✉

The integration of CO_2 into the dehydrogenation of propane (PDH) holds significant promise for both propylene production and greenhouse gas utilization. However, a pivotal challenge lies in mitigating the undesirable dry reforming of propane (DRP), which diminishes propylene selectivity compared to direct PDH processes. Herein, we describe a coupled process that integrates PDH with reverse water gas shift (RWGS) using a tandem catalytic system. The $PtSn/Al_2O_3$ analogue performs the dehydrogenation reaction, while an adjacent defective CeO_x/Al_2O_3 at nanoscale acts as the hydrogenation sites for CO_2. Catalysis and kinetic studies demonstrate the in-situ removal of hydrogen from $PtSn/Al_2O_3$ to adjacent CeO_x/Al_2O_3, facilitated by CO_2, shifts the quasi-equilibrium of PDH towards propylene production, while suppressing the competitive DRP side reaction. This hydrogen spillover-mediated coupling mechanism enables superior propylene selectivity of ~98.8%, along with high CO_2 (~43.9%) and propane conversion (~44.2%) at 550 °C, outperforming direct PDH (~40.6%). Analysis of CO_2 footprint indicates the PDH-RWGS tandem process has the potential for carbon utilization to mitigate detrimental CO_2 emissions.

Propylene is a vital building block for producing a wide range of high-value-added chemicals. Propane dehydrogenation (PDH) represents an on-purpose technology that produces propylene[1,2]. However, the reaction is intensely endothermic[3,4]. Oxidative dehydrogenation of propane (ODHP) using O_2 as oxidant has been proposed to overcome equilibrium limitations, but it suffers from overoxidation[5,6], giving yields below the PDH equilibrium[7–9]. Carbon dioxide (CO_2), a greenhouse gas, can act as a soft oxidant during PDH to lower ΔG for the reaction and make the reaction feasible at lower operating temperature[10,11]. This not only facilitates the reaction but also presents a promising strategy for mitigating CO_2 emissions[12]. Meanwhile, in the CO_2-ODHP system, carbon deposition can be eliminated through the reverse Boudouard reaction ($CO_2 + C = 2CO$). Although desirable, this reaction has proven challenging, as most catalysts for CO_2-ODHP tend to undergo severe dry reforming side reactions[13].

Previous studies focused on the design of bifunctional catalysts for the coactivation of propane and CO_2[14–17]. Reducible metal ions readily donate abundant lattice O atoms to allow efficient turnover due to their redox and acidic nature. However, the oxides possess limited ability for C-H cleavage and exhibit short life cycles[10]. Comparatively,

[1]Key Laboratory for Green Chemical Technology of Ministry of Education, School of Chemical Engineering & Technology, Collaborative Innovation Center for Chemical Science & Engineering, Tianjin University, Tianjin 300072, China. [2]International Joint Laboratory of Low-carbon Chemical Engineering of Ministry of Education, Tianjin 300350, China. [3]Joint School of National University of Singapore and Tianjin University, International Campus of Tianjin University, Binhai New City, Fuzhou 350207, China. [4]Haihe Laboratory of Sustainable Chemical Transformations, Tianjin 300192, China. [5]National Industry-Education Platform of Energy Storage, Tianjin University, Tianjin 300350, China. [6]Zhejiang Institute of Tianjin University, Ningbo, Zhejiang 315201, China. [7]Tianjin Normal University, Tianjin 300387, China. [8]State Key Laboratory of Synthetic Biology, Tianjin University, Tianjin 300072, China. [9]These authors contributed equally: Kaige Tian, Sai Chen, Guodong Sun. ✉e-mail: chunlei.pei@tju.edu.cn; jlgong@tju.edu.cn

https://doi.org/10.1038/s41467-025-65261-6

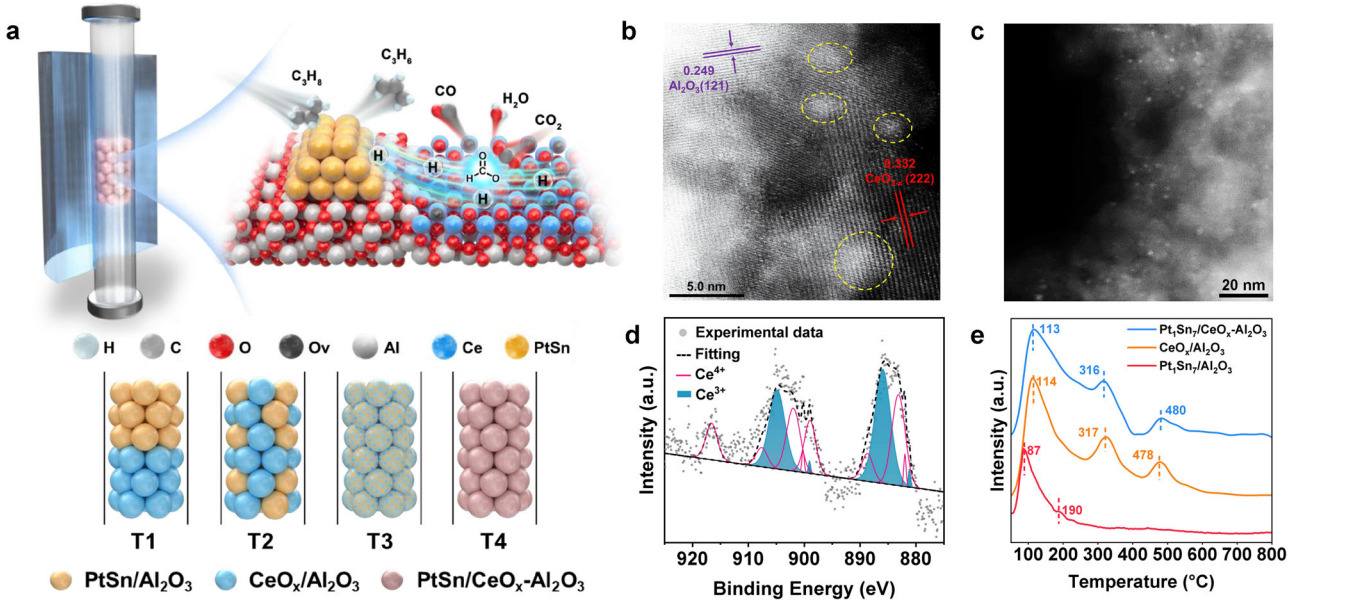

Fig. 1 | Tandem systems for PDH-CO_2 hydrogenation process. a Tandem catalysts in different modes: T1 (dual-bed): Upper bed: Pt_1Sn_7/Al_2O_3 (20–40 mesh, 0.35–0.833 mm), lower bed: CeO_x/Al_2O_3 (20–40 mesh); T2 (granule-mix): Physical mixture of Pt_1Sn_7/Al_2O_3 and CeO_x/Al_2O_3 (both 20–40 mesh); T3 (powder-mix): Pt_1Sn_7/Al_2O_3 and CeO_x/Al_2O_3 separately ground to 0.05–0.075 mm, physically mixed, tableted and re-sieved to 20–40 mesh; T4 (mortar-mix): Pt_1Sn_7/CeO_x-Al_2O_3 tandem catalyst, sieved to 20–40 mesh. **b** The representative AC-HAADF-STEM image and (**c**) HAADF-STEM images of Pt_1Sn_7/CeO_x-Al_2O_3 tandem catalyst (T4). **d** Ce 3*d* XPS spectra of Pt_1Sn_7/CeO_x-Al_2O_3 tandem catalyst (T4). and **e** CO_2-TPD profiles of Pt_1Sn_7/Al_2O_3, CeO_x/Al_2O_3 and Pt_1Sn_7/CeO_x-Al_2O_3 tandem catalyst (T4). The a.u. stands for arbitrary units.

Xing et al. reported a Pt-Co-In ternary nanoalloy that demonstrates high C_3H_6 selectivity and CO_2 utilization[18]. However, the alloy structure's inability to distinctly segregate the C-H bond activation sites from the C = O bond activation sites results in competitive adsorption and promotes dry reforming of propane (DRP). The similar results were reported by Zhai et al.[19] on $PtSn/SiO_2$ catalysts that highlight the metal-oxide interface (i.e., Pt_3Sn-SnO_x) as active sites for propane dehydrogenation and reverse water gas shift (RWGS) reaction. However, the mechanistic understanding on the diffusion of reactive intermediates between tandem catalytic sites remains challenging[20]. At the process engineering level, the utilization of membrane reactors and chemical looping is anticipated to bolster propylene selectivity through the physical or temporal segregation of dehydrogenation and CO_2 hydrogenation[21–24]. However, the implementation of these technologies poses certain challenges in scaling up reactor and processes.

Herein, we develop a coupling process that integrates PDH and RWGS and demonstrate the thermodynamic/kinetic matching of PDH and RWGS steps by regulating the spillover of hydrogen intermediates over the designed tandem catalyst (Fig. 1a). The well-established PDH catalyst, $PtSn/Al_2O_3$ provides the dehydrogenation sites, while adjacent CeO_x/Al_2O_3 at the nanoscale acts as the hydrogenation sites for subsequent RWGS reaction. We achieved a high propylene selectivity of 98.8%, accompanied by high CO_2 (44.0%) and propane conversion (44.2%) at 550 °C surpassing that via direct PDH. Based on catalytic experiments, spectroscopic characterization, and kinetic studies, we propose a hydrogen spillover-mediated coupling mechanism. The hydrogen species generated at the $PtSn/Al_2O_3$ sites migrated to adjacent CeO_x/Al_2O_3 for the RWGS reaction, thereby driving PDH towards propylene production. This mechanism is favored by the proximity between the dehydrogenation and hydrogenation sites.

Results and Discussion

Design of tandem catalysts

We initially performed thermodynamic calculations for DRP, PDH, direct and indirect pathway of CO_2-PDH (Supplementary Fig. 1)[25,26]. At 550 °C, the equilibrium conversion of CO_2 for DRP can reach up to 99.8%, while no C_3H_6 is formed. The direct pathway of CO_2-PDH can reach an equilibrium conversion of C_3H_8 of 33.0% as opposed to 56.8% for PDH. Comparatively, the tandem reaction of CO_2 with C_3H_8 (indirect pathway) increases the equilibrium conversion of C_3H_8 to 63.9% by consuming H_2 through the RWGS reaction.

Based on the thermodynamic analysis, we investigated the different tandem configurations of dehydrogenation catalysts and RWGS catalysts within a single reactor (Fig. 1a). Given the established advantages of supported PtSn[27] and CeO_x[28] have been in activation of propane and CO_2, respectively, these were chosen as the PDH and RWGS catalysts for this study. The tandem models, labeled T1 to T4, correspond to different contact distances between the catalysts, ranging from millimeters to nanometers[29].

In tandem mode T1 (dual-bed), $PtSn/Al_2O_3$ and CeO_x/Al_2O_3 pellets are loaded into the reactor by means of upper and lower bed filling. In T2 (granule-mix), the two catalyst pellets are mixed and loaded into the reactor. In T3 (powder-mix), the two catalysts are fully milled into a fine powder, pressed, and sieved to produce pellets for reactor loading. In T4 (mortar-mix), nanoscale contact between PtSn nanoparticles and CeO_x/Al_2O_3 is achieved by impregnating a mixed solution of Pt and Sn precursors onto CeO_x/Al_2O_3, resulting in a composite catalyst denoted as $PtSn/CeO_x$-Al_2O_3.

The $PtSn/CeO_x$-Al_2O_3 tandem catalyst (T4) was characterized in details. X-ray diffraction (XRD) patterns (Supplementary Fig. 2) and aberration-corrected high-angle annular dark-field scanning transmission electron microscopy (AC-HAADF-STEM) images revealed the presence of oxygen-deficient CeO_x within the T4 tandem catalysts (Fig. 1b). This was further corroborated by the formation of a significant density of Ce^{3+} species, as evidenced by X-ray photoelectron spectroscopy (XPS)[30,31] (Fig. 1d), Additionally, highly dispersed PtSn nanoparticles (Fig. 1b, c), measuring approximately 2.0 ± 0.5 nm (Supplementary Fig. 3b–g), adorned the surface[32,33]. The CO_2-TPD profiles (Fig. 1e) exhibited CO_2 desorption peaks at approximately 316 °C and 480 °C on CeO_x/Al_2O_3 and $PtSn/CeO_x$-Al_2O_3, respectively, indicating the presence of additional activation sites for CO_2 on the $PtSn/CeO_x$-Al_2O_3 tandem catalyst compared to the $PtSn/Al_2O_3$

https://doi.org/10.1038/s41467-025-65261-6

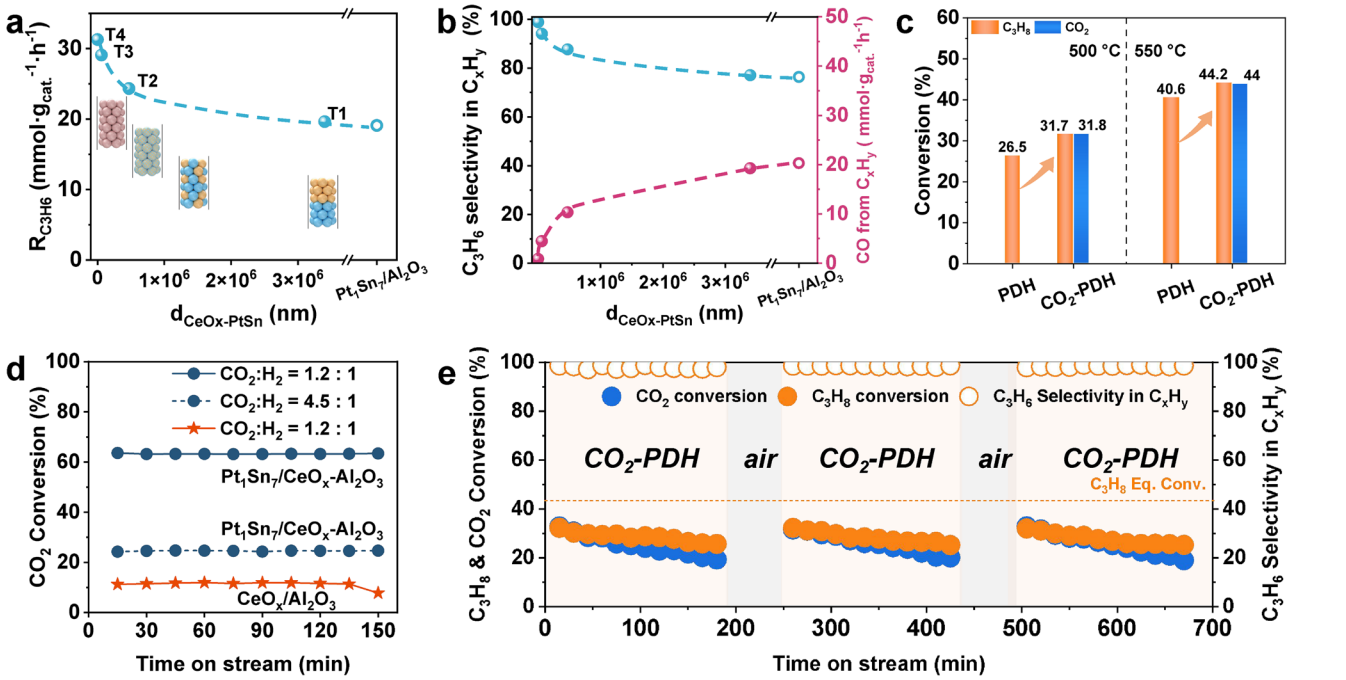

Fig. 2 | Catalytic performance of tandem catalysts. a, b Catalytic performance at different distances between $PtSn/Al_2O_3$ and CeO_x/Al_2O_3 at 500 °C. **c** Initial conversion of C_3H_8 and CO_2 at 15 minutes of PDH and CO_2-PDH at 500 °C and 550 °C on Pt_1Sn_7/CeO_x-Al_2O_3 tandem catalyst (T4). Catalytic testing conditions of (**a**–**c**): integral reactor, atmospheric pressure, 150 mg catalyst, WHSV of propane = 4.6 h^{-1}, C_3H_8: CO_2: N_2 = 5: 3: 27 mL·min^{-1}. **d** RWGS on Pt_1Sn_7/CeO_x-Al_2O_3 tandem catalyst (T4) at 550 °C. Catalytic testing conditions: atmospheric pressure, 150 mg catalyst, CO_2: H_2: N_2 = 6: x: (29-x) mL·min^{-1}. **e** Cyclic stability testing with Pt_1Sn_7/CeO_x-Al_2O_3 tandem catalyst (T4), regeneration: 45 min regeneration at 500 °C in flowing 20% O_2/N_2 (35 mL·min^{-1}), and 1 h reduction at 500 °C in flowing 40% H_2/N_2 (35 mL·min^{-1}).

catalyst[34,35]. Furthermore, we confirmed that the CO_2 chemical adsorption capacity is significantly enhanced with increasing Ce^{3+} concentration, which verifies that oxygen vacancies might serve as the primary sites for CO_2 activation (Supplementary Fig. 4).

Proximity-dependent propylene selectivity and formation rates

We demonstrated the application of tandem catalysts in a continuous process scheme for PDH followed by CO_2 hydrogenation. The outlet gas was analyzed and found to contain CH_4, C_2H_6, C_2H_4, C_3H_6, CO, H_2O, and H_2 (Supplementary Fig. 5). When using $PtSn/Al_2O_3$ catalysts, the CO_2 conversion remained relatively unchanged as the molar ratio of Sn to Pt was varied (Supplementary Fig. 6a). However, the contribution of dry reforming, in terms of CO production from hydrocarbons, exhibited a reverse volcano peak relationship, reaching a minimum value of 20.3 mmol·g_{cat}^{-1}·h^{-1} at an optimized Sn to Pt ratio of 7 (Supplementary Fig. 6b).

Inter-particle distances were computationally analyzed using MATLAB with Monte Carlo method (Supplementary Fig. 7 and Supplementary Table 1). A granular mixture (T2) of CeO_x/Al_2O_3 and $PtSn/Al_2O_3$ resulted in a decreased CO production from hydrocarbons (10.3 mmol·$g_{cat.}^{-1}$·h^{-1}) and a higher propylene production rate (24.3 mmol·$g_{cat.}^{-1}$·h^{-1}) compared to Pt_1Sn_7/Al_2O_3 (Fig. 2a, b and Supplementary Fig. 8). For the $PtSn/CeO_x$-Al_2O_3 tandem catalyst (T4), which exhibited nanoscale intimacy, the propylene formation rate was further enhanced to 31.3 mmol·$g_{cat.}^{-1}$·h^{-1}, with the lowest CO production from C_3H_8 (0.87 mmol·$g_{cat.}^{-1}$·h^{-1}) and the highest propylene selectivity in C_xH_y (C_3H_6, CH_4, C_2H_6, C_2H_4) of 98.8%. The strong correlation between the proximity of $PtSn/Al_2O_3$ and CeO_x/Al_2O_3 and the propylene selectivity suggested effective communication between the tandem catalysts. This result aligns with the notion that "the closer-the better" in terms of catalyst intimacy[36].

We further demonstrated the superiority of the tandem catalysts in PDH-CO_2 hydrogenation when compared to direct PDH. At 500 °C and WHSV of propane (4.6 h^{-1}), the initial propane conversion was 31.7%, which was higher than that observed for the direct PDH reaction (26.5%) (Fig. 2c). Notably, the CO_2 conversion exceeds the equilibrium conversion at the corresponding temperatures (Supplementary Fig. 1: 25.8% at 500 °C, 35.4% at 550 °C). This deviation might be attributed to the additional consumption of CO_2 by the DRP, However, as shown in Supplementary Table 2, the experimented ratios of CO/CO_2 and CO/C_3H_8 are closer to the thermodynamic equilibrium values when the PDH-RWGS pathway dominates, and the higher C_3H_6 to H_2 ratio and lower H_2 partial pressure at the outlet in CO_2-PDH (1.7) versus PDH (0.9) at 500 °C (Supplementary Fig. 9a), meanwhile, the relevant methanation reactions (*i.e.* CH_4 formation rate) are essentially negligible (Supplementary Fig. 9b, c), which further indicated the in-situ consumption of H_2 through the PDH-RWGS pathway.

Although the reaction primarily follows the PDH-RWGS pathway, the reaction network exhibits significant temperature dependence, as shown in Supplementary Fig. 10a, b, a systematic evaluation of the temperature ranges from 500 to 600 °C revealed that the conversions of C_3H_8 and CO_2 significantly increase due to endothermic nature of this reaction. However, accelerated catalyst deactivation at higher temperatures leads to a decline in propane conversion. Meanwhile, propylene selectivity gradually decreases with rising temperature, which is attributed to the thermodynamic favorability of the dry reforming reaction ($C_3H_8 + 3CO_2 \rightarrow 6CO + 4H_2$, $\Delta H = +620$ kJ/mol). As illustrated in Supplementary Fig. 10c, the partial pressure ratio of C_3H_6 to H_2 at the reactor outlet decreases progressively with increasing temperature, confirming that dry reforming or coke formation competitively consumes propane and suppresses propylene yield.

To investigate the catalyst deactivation mechanism, RWGS tests were conducted within the different hydrogen partial pressures observed during the C_3H_8 and CO_2 reaction (Fig. 2d). The $PtSn/CeO_x$-Al_2O_3 tandem catalysts (T4) exhibited remarkable stability, which suggests that catalyst deactivation is not caused by restructuring induced by CO_2. Rather, carbon deposition, likely resulting from the in-situ removal of H_2 during PDH, is the primary cause of catalyst

https://doi.org/10.1038/s41467-025-65261-6

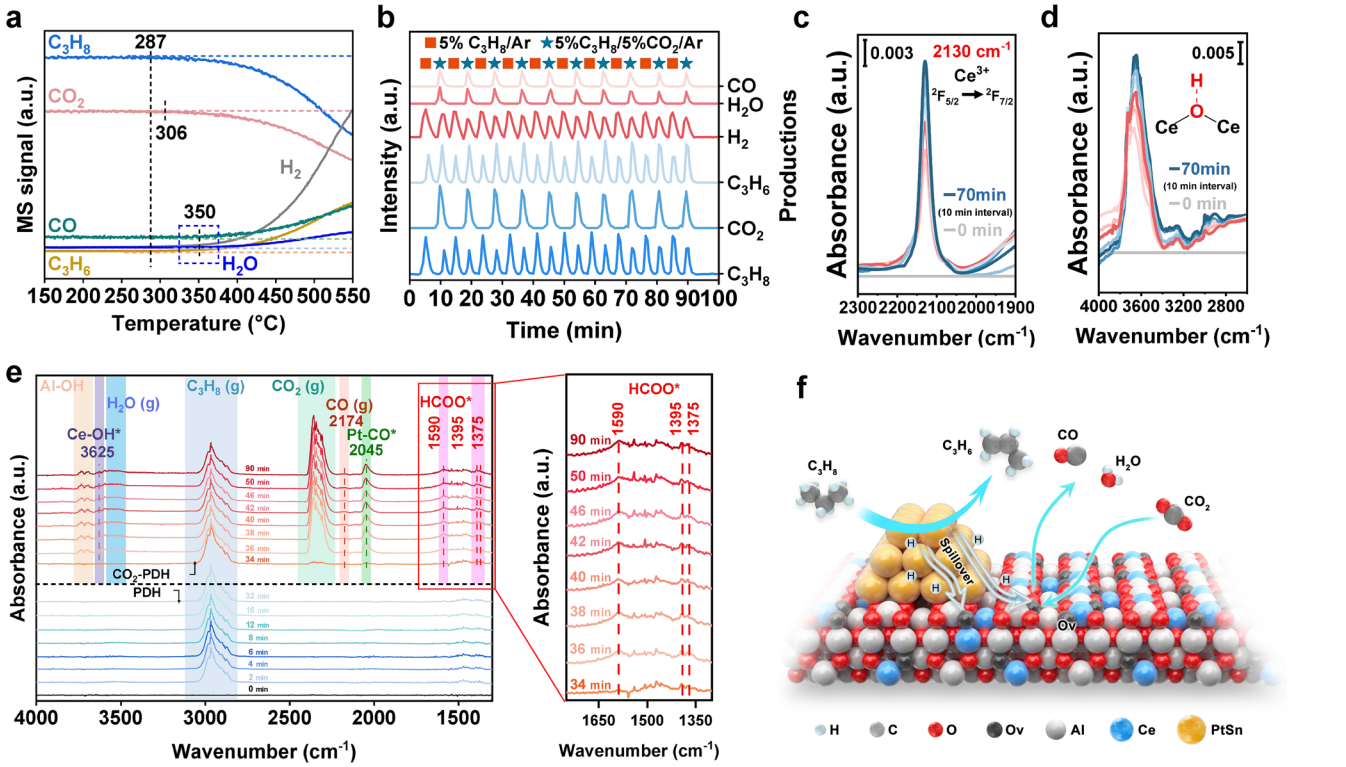

Fig. 3 | Evidence of hydrogen spillover–coupling mechanism of PDH with RWGS on Pt_1Sn_7/CeO_x-Al_2O_3 tandem catalyst (T4). a TPSR in CO_2-PDH reaction atmosphere on fixed-bed reactor. **b** Pulse experiment in PDH and CO_2-PDH reaction atmosphere. **c**, **d** DRIFTS spectra of 10% H_2/Ar. **e** In-situ DRIFTS spectra of CO_2-PDH reaction atmosphere. **f** Schematic illustration of the reaction mechanism of PDH-RWGS on PtSn/CeO_x-Al_2O_3 (T4) in PDH-CO_2 hydrogenation process. The a.u. stands for arbitrary units.

deactivation (Supplementary Fig. 11). Notably, the PtSn/CeO_x-Al_2O_3 tandem catalyst fully recovered and maintained its initial C_3H_8 conversion, C_3H_6 selectivity (including hydrocarbon and net selectivity), and CO_2 conversion after undergoing three consecutive cycles (Fig. 2e, Supplementary Fig. 12). Furthermore, experimental results under different propane concentrations indicate that propane conversion exhibits a non-monotonic decline with increasing propane concentration (Supplementary Fig. 13), while propylene selectivity remains unchanged, even at a higher pre-reduction temperature of 600 °C, the catalyst demonstrates stable performance and regeneration capability (Supplementary Figs. 14, 15). These findings further improve its adaptability potential for industrial applications.

The role of hydrogen spillover in coupling PDH and RWGS

To investigate the promotion effect of CO_2 on PDH, catalysis studies focusing on C-H bond activation were carried out. For the C_3H_8 temperature-programmed surface reaction (TPSR), the similar initial activation temperatures observed on PtSn/Al_2O_3 (279 °C) and PtSn/CeO_x-Al_2O_3 tandem catalysts (282 °C) indicate that the tandem system does not alter the catalyst's ability to activate C-H bonds (Supplementary Fig. 16). This similarity is further supported by the comparable geometric and electronic states of Pt in both PtSn/Al_2O_3 and PtSn/CeO_x-Al_2O_3 tandem catalysts, as evidenced by the similar CO adsorption band at 2083 cm^{-1} on Pt top sites, as detected by CO-diffuse reflectance infrared Fourier transform spectroscopy (DRIFTS) (Supplementary Fig. 17a, b)[37]. Furthermore, we demonstrated that the CO adsorption band on PtSn/CeO_x-Al_2O_3 catalyst showed negligible changes before and after regeneration across different reactions (PDH, CO_2-PDH, and RWGS, Supplementary Fig. 17c).

We noted that when C_3H_8 and CO_2 were co-fed into the reactor, the temperatures for CO_2 consumption (306 °C) and CO formation (350 °C) were higher than the initial C-H activation temperature of propane (287 °C) (Fig. 3a). Furthermore, isothermal pulse experiments conducted at 500 °C by continuously switching between 5% C_3H_8/95% Ar and 5% CO_2/5% C_3H_8/90% Ar atmospheres (Fig. 3b) revealed that upon introduction of CO_2, the intensities of C_3H_8 and H_2 decreased, while the intensities of C_3H_6 increased immediately, accompanied by the formation of CO and H_2O. These observations suggest that C-H bond activation precedes the activation of the C=O bond, leading to the generation of CO and H_2O. We hypothesize that H*, the product of C-H activation, serves as a crucial intermediate that links the PDH and RWGS reactions through a surface diffusion mechanism.

We then performed H_2 temperature-programmed reduction (H_2-TPR) and H_2 temperature-programmed desorption (H_2-TPD) to investigate the spillover of hydrogen species. PtSn sites can dissociate H_2 to generate active hydrogen atoms (H*) (the first reduction peak at 199–232 °C), which spillover to the CeO_x surface, significantly reducing the reduction temperature of CeO_x. As shown in Supplementary Fig. 18a and Supplementary Table 3, among different configurations, as the PtSn-CeO_x interfacial distance progressively decreases (from T1 to T4), the closely contacted mortar-mix (T4) exhibits the lowest reduction temperature (346 °C), whereas the physically separated dual bed (T1) relies on gaseous hydrogen transfer, resulting in a higher reduction temperature (491 °C). Notably, in configurations T1 to T3, the Pt source responsible for the initial H_2 dissociation is the same Pt_1Sn_7/Al_2O_3 catalyst. In addition, the Pt_1Sn_7/CeO_x-Al_2O_3 and Pt_1Sn_7/Al_2O_3 catalysts exhibit identical particle size distributions (Supplementary Fig. 19) and share the same Pt coordination environment. This ensures consistent morphology of the Pt species when comparing the reduction behaviors across T1 to T4. Therefore, the observed differences in reduction temperatures can be attributed to variations in the spatial configuration between the PtSn active sites and the CeO_x reduction sites[38]. Moreover, as the inter-site distance narrows, hydrogen consumption gradually increases from T1 (0.27 $cm^3/g_{cat.}$) to T4 (1.62 cm^3/

$g_{cat.}$), which further demonstrates that the hydrogen spillover effect promotes reduction of the CeO_x. For H_2-TPD (Supplementary Fig. 18b), on mortar-mix (T4) mode, the first H_2 desorption peak (~42 °C) is attributed to the H* on the Pt, and the second H_2 desorption peak (~287 °C) is attributed to the spillover hydrogen on the interface between PtSn particles and CeO_x/Al_2O_3, and the other one at higher temperature (>600 °C) is attributable to H* in the subsurface region and spillover hydrogen on CeO_x/Al_2O_3 support[39–41]. Qualitative analysis revealed that as the distance between PtSn particles and CeO_x/Al_2O_3 decreases, the intensity of desorption peaks of spilled hydrogen gradually increases, further demonstrating the importance of site proximity for the hydrogen spillover.

Previous results demonstrated that on pure CeO_2, H_2 primarily undergoes heterolytic dissociation, with H_2O formation limited by converting heterolytic to homolytic products[42]. In Pt/CeO_2, H_2 dissociates homolytically on Pt, followed by rapid hydrogen spillover, leading to approximately double the OH_{ads}^- coverage compared with pure CeO_2[43–46]. The DRIFTS spectra under H_2 flow showed a simultaneous increase in [OH_{ads}^-] (3000–3500 cm^{-1}) and the forbidden $^2F_{5/2}$-to-$^2F_{7/2}$ electronic transition of Ce^{3+} (2130 cm^{-1}) (Fig. 3c, d and Supplementary Fig. 20). This correlation indicates that PtSn promotes the spillover of homolytic dissociation hydrogen species onto the CeO_x surface, as described by the determined $d[OH_{ads}^-]/dt = k \times d[Ce^{3+}]/dt$ (where k is a positive constant)[47–50]. In contrast, without PtSn nanoparticles, the DRIFTS profile of the CeO_x/Al_2O_3 under the same conditions showed that [Ce^{3+}] increased continuously with H_2 reduction time (Supplementary Fig. 21), while [OH_{ads}^-] increased only within 10 minutes and remained essentially unchanged. This provides direct evidence that Pt facilitates the spillover of dissociated hydrogen species onto the CeO_x surface[50].

In-situ DRIFTS was further performed to monitor the evolution of intermediates during the coupling reaction of PDH and RWGS. As shown in Fig. 3e and Supplementary Figs. 22, 23, for $PtSn/CeO_x$-Al_2O_3 tandem catalysts, characteristic bands assigned to gaseous C_3H_8 (2810–3060 cm^{-1}) were detected in the initial stage during PDH reaction[51,52]. Upon switching the feed from C_3H_8/Ar to C_3H_8/CO_2/Ar, CO adsorbed on Pt at 2045 cm^{-1} was detected together with H_2O (3470–3580 cm^{-1}), Ce-OH (3625 cm^{-1}) and Al-OH (3665–3770 cm^{-1})[53–55], respectively, suggesting the RWGS occurs during the reaction. It is noteworthy that the characteristic peaks of the HCOO* intermediate (1590 cm^{-1}, 1395 cm^{-1}, 1375 cm^{-1}) were observed simultaneously. Previous research showed that alternative intermediates such as $*CH_3CH_2CH_2$, $*CH_3CHCH_2$, and $*CH_3CH_2$ could react with *O derived from CO_2 to form $*CH_3CH_2CH_2O$, $*CH_3CH_2CHO$, and $*H_2O$ instead of involving the formation of formate acting as hydrogen donors[56–58]. Therefore, the formation of formate species should originate from the reaction between CO_2 and dissociated hydrogen species (H*) derived from C–H bond cleavage of propane. These results suggest that a coupled PDH-RWGS pathway is dominated, and H_2 produced by PDH on $PtSn/Al_2O_3$ can spillover to the adjacent CeO_x/Al_2O_3 (Fig. 3f), which results in a subsequent RWGS reaction.

Kinetic studies and KIE experiments

We performed a kinetic study using a differential reactor to understand in depth the functions of tandem catalysis with the exclusion of internal and external diffusion and temperature gradients. More detailed experimental details are given in the supplementary information (Kinetic analysis of CO_2-PDH, PDH and RWGS, Supplementary Figs. 24–30, Supplementary Tables 4–8). The initial reaction rates were obtained by correcting the equilibrium and deactivation[59].

Across a broad range of partial pressures of C_3H_8 (0–30 kPa), and H_2 (0–40 kPa), the tandem systems achieved the higher propylene formation rates when co-feeding CO_2 than that of PDH (Fig. 4a–c). A kinetic analysis was conducted to understand the rate-determining step (RDS) of the PDH and CO_2-PDH (see Supplementary Information: Kinetic analysis of PDH and CO_2-PDH section). Prior to analyzing the CO_2-PDH reaction system, kinetic studies of the RWGS reaction over the Pt_1Sn_7/CeO_x-Al_2O_3 catalyst, combined with theoretical analyses based on Langmuir-Hinshelwood (L-H) and Mars-van Krevelen (MvK) mechanistic assumptions, indicate that the $CO_2 + H^*$ reaction in this work follows the L-H mechanism (see Supplementary Information: Kinetic analysis of RWGS section). So we considered a L-H mechanism involving a two-step dehydrogenation of C_3H_8 to C_3H_6. Subsequently, CO_2 is reduced via hydrogen derived from propane dehydrogenation through the formate pathway to produce CO, with the hydrogen eliminated in the process being oxidized to form water[18]. We solved the rate equation of each step by applying the quasi-steady-state approximation and site conservation conditions[60].

The experimental reaction order with respect to C_3H_8 was found to be 1.24 for CO_2-PDH and 1.18 for PDH (Fig. 4a), whereas the reaction order with respect to CO_2 was determined to be 0.44 in the range of 0–8.6 kPa, and close to 0 in the range of 8.6–34.4 kPa (Fig. 4b). This suggests that at low CO_2 partial pressures (<8.6 kPa), the hydrogen generated from PDH is efficiently consumed by the tandem reaction, resulting in enhanced propylene production. However, since the reaction exhibits zero-order kinetics with respect to CO_2 when its partial pressure exceeds 8.6 kPa, further increasing the CO_2 partial pressure does not enhance the formation rate of C_3H_6 reaction rate. Furthermore, the negligible influence of co-feeding CO with C_3H_8/CO_2 rules out the possibility of CO inhibition, likely due to its limited surface coverage at high temperatures (Supplementary Fig. 31). The predicted rates were in agreement with the experimental data (Fig. 4d) only when the second C-H cleavage of propane was considered as the RDS for CO_2-PDH (Supplementary Fig. 24).

We further investigated the tandem reaction mechanism with kinetic isotopic experiments (KIE). As shown in Fig. 4e, a normal KIE value of 2.7 (r_H/r_D) was observed when switching from C_3H_8 to C_3D_8 after reaching the steady state on $PtSn/CeO_x$-Al_2O_3[61], while KIE value equals to 0.99 (r_{12_C}/r_{13_C}) by switching $^{12}CO_2$ to $^{13}CO_2$, which validated that the kinetic relevance of C-H activation was the RDS[62,63]. The apparent activation energy (*Ea*) was estimated for $PtSn/Al_2O_3$ and $PtSn/CeO_x$-Al_2O_3 tandem catalyst by Arrhenius-type plots. The *Ea* of PDH has essentially the same values (84.4 and 85.4 kJ•mol^{-1}) for both catalysts (Supplementary Fig. 33). This suggests that the incorporation of CeO_x did not alter the activation capacity of $PtSn/Al_2O_3$ for C-H bonds, which is also consistent with previously reported results for C_3H_8-TPSR and CO-DRIFTS. However, the *Ea* of CO_2-PDH was significantly reduced (from 96.7 to 73.6 kJ·mol^{-1}) by the incorporation of CeO_x into Pt_1Sn_7/Al_2O_3, which validates that the tandem process can promote the dehydrogenation during the co-feeding of CO_2 with C_3H_8.

Related tandem catalysts

To extend the coupling of PDH and RWGS through hydrogen spillover, we investigated tandem catalysts from two perspectives: by modifying either the PDH catalysts ($PtSn/Al_2O_3$, GaO_x/Al_2O_3, CrO_x/Al_2O_3) or the CO_2 hydrogenation catalysts (CeO_x/Al_2O_3, Cu/Al_2O_3, TiO_x/Al_2O_3) in intimate tandem configurations, as mentioned earlier (Supplementary Fig. 34). As anticipated, we observed enhanced propylene production rates compared to the parent rates without tandem coupling. These findings support the hydrogen spillover-mediated coupling mechanism in a tandem setup, emphasizing the importance of proximity between the two reaction sites.

Analysis of CO_2 footprint

The superiority of PDH-CO_2 hydrogenation tandem process to PDH implies the potential application for propylene synthesis[25,64,65]. To analyze the additional separation processes introduced by CO_2 in the PDH-CO_2 hydrogenation tandem process compared to conventional PDH, we incorporated two additional PSA units to achieve H_2/CO and CO_2/C_2 separation functionalities. The separated CO_2 is recycled back

https://doi.org/10.1038/s41467-025-65261-6

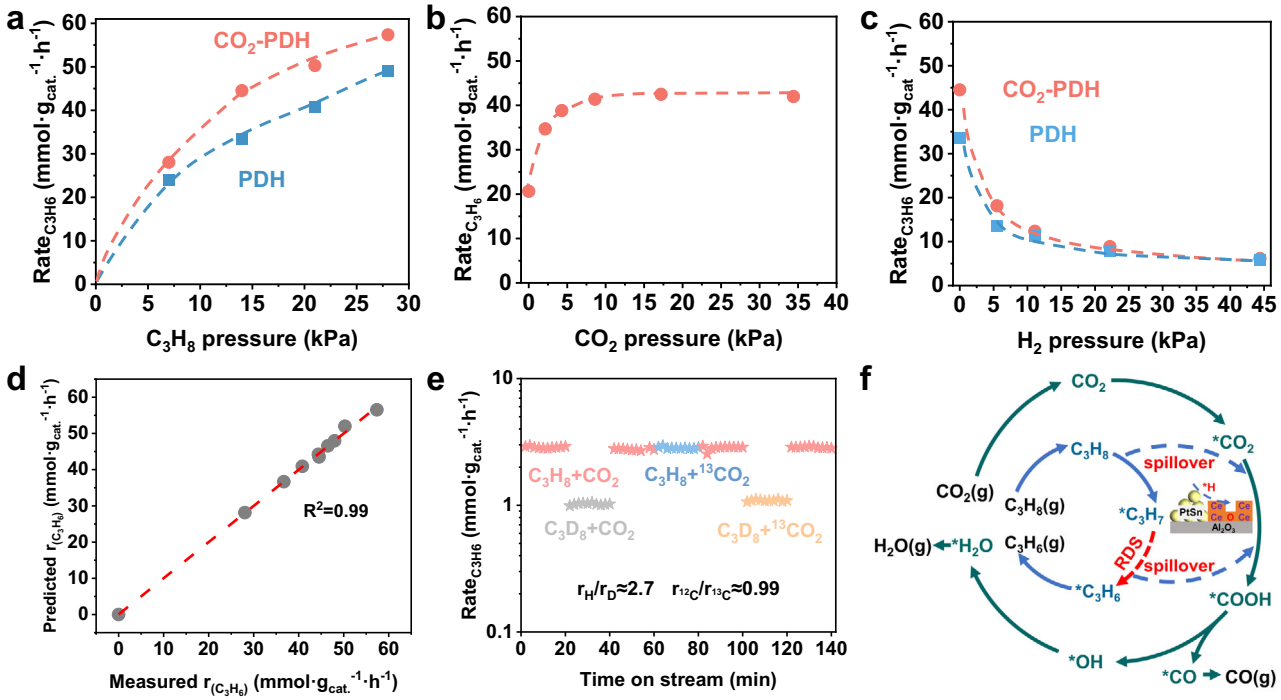

Fig. 4 | Kinetics of hydrogen spillover–coupling mechanism of PDH with RWGS. **a**–**c** CO_2-PDH and PDH under different C_3H_8, CO_2 and H_2 partial pressures. The dash lines are to guide the eyes. Catalytic testing conditions: 500 °C, differential reactor, atmospheric pressure, 50 mg Pt_1Sn_7/CeO_x-Al_2O_3 tandem catalyst (T4). **a** C_3H_8: 7–28 kPa, CO_2: 8.6 kPa; (**b**) C_3H_8: 9 kPa, CO_2: 0–34.4 kPa; (**c**) C_3H_8: 14 kPa, CO_2: 8.6 kPa, H_2: 0–44.4 kPa, 35 mL·min^{-1} total flow rate balanced with N_2 (detail data from Supplementary Figs. 26–30). **d** Comparison of predicted (from Supplementary Eq. S(63)) and experimental C_3H_6 formation rates. **e** KIEs of CO_2-PDH on Pt_1Sn_7/CeO_x-Al_2O_3 tandem catalyst (T4) (detail data from Supplementary Fig. 32). **f** Proposed reaction processes of hydrogen spillover-coupling mechanism of PDH with RWGS.

into the feed stream. We then compared the net CO_2 emissions and energy consumption for both (Supplementary Tables 9–13 and Supplementary Figs. 35, 36). The PDH-CO_2 hydrogenation tandem process for producing C_3H_6 requires more energy (21.09 GJ/ton of propylene) compared with the Oleflex PDH process (17.78 GJ/ton of propylene). However, due to the increased consumption of CO_2 by the PDH-CO_2 hydrogenation tandem process, its net CO_2 emissions are approximately 0.69 ton/ton of propylene, which is much lower than that of the Oleflex PDH process (1.23 ton/ton of propylene). This indicates that PDH-CO_2 hydrogenation tandem process is a promising strategy for carbon utilization to mitigate CO_2 emissions. Future advancements might focus on enhancing catalyst efficiency or integrating co-conversion reactions where CO_2-PDH products directly feed downstream reactions, which might enable bypassing complex and energy-intensive separation processes.

To conclude, we propose the coupled pathway of PDH-RWGS over tandem catalysts consisting of dehydrogenation sites, *i.e.* $PtSn/Al_2O_3$ and CO_2 hydrogenation sites, *i.e.* CeO_x/Al_2O_3. This tandem configuration effectively mitigates the competitive dry reforming reaction associated with PDH, resulting in a high propylene selectivity of 98.8%. In-situ characterizations and kinetic analysis have revealed that hydrogen (H) serves as a crucial intermediate in coupling PDH and RWGS. The industrial manufacture of tandem catalysts with atomic-level control of different active sites needs substantial development to provide this technology for the olefin industry.

Methods

Materials properties and synthesis

All the catalysts were prepared by incipient wetness impregnation method. Methods of CeO_x/Al_2O_3(10 wt.% CeO_2) preparation based on Xie's work[66], In details, the $Ce(NO_3)_3{\cdot}6H_2O$ (99.0%, Aladdin biological technology Co., Ltd. (Shanghai, China)) solution with determined concentration was added dropwise onto γ-Al_2O_3 (Adamas-beta reagent Co., Ltd. (Shanghai, China)) under stirring. The obtained wet powder was dried at 120 °C for 1 h and then calcined in air at 550 °C for 2 h. Subsequently, the CeO_x/Al_2O_3 support was obtained by reducing the base support in 10% H_2/Ar flow at 750 °C for 2 h with a temperature ramp of 5 °C/min. For the synthesis Pt_1Sn_x/CeO_x-Al_2O_3 (the loading of Pt atoms is fixed at 0.15 wt.% into CeO_x/Al_2O_3, and x = 1, 3, 5, 7, 10, 15. Here x represents the molar ratio of Sn/Pt), $H_2PtCl_6{\cdot}6H_2O$ (Chemart (Tianjin) Chemical Technology Co., Ltd, 99.9%) and $SnCl_2{\cdot}2H_2O$ (Chemart (Tianjin) Chemical Technology Co., Ltd, 99.9%) were added to a 0.1 M HCl solution and used as precursors. The precursors solution with determined concentration of Pt and Sn was dropwise onto CeO_x/Al_2O_3. After impregnation, the catalysts were placed in the atmosphere statically overnight and then dried in the flowing air at 80 °C for 12 h and then calcined at 600 °C for 2 h.

Catalytic testing

The catalytic testing was performed in a quartz fixed-bed reactor with 8 mm inner diameter and 24 cm length at atmosphere pressure. A mixture of 150 mg catalysts and 0.1 mL quartz sand with 20–40 mesh-size distribution was loaded in the quartz tubular reactor. The catalysts were first heated to 600 °C at a rate of 10 °C·min^{-1} in N_2 (35 mL·min^{-1}). After heating to 600 °C, the catalysts were treated in H_2/N_2 (40% H_2/N_2, 35 mL·min^{-1}) for 1 h and then purged in N_2 (35 mL·min^{-1}) for another 30 min, meanwhile, reduce the reaction temperature to 500/550 °C. Afterwards, the reactant gas [C_3H_8: N_2 = 1: 6 or CO_2: C_3H_8: N_2 = x: 1: (6-x), total flow rate is 35 mL·min^{-1}] was fed into the reactor. The gas products were analyzed by an online GC (Shimadzu GC-2014C) what integrated with double detectors: the thermal conductivity detector for H_2, N_2, CO and CO_2, and the flame ionization detector for hydrocarbons, such as CH_4, C_2H_6, C_2H_4, C_3H_8, and C_3H_6, where N_2 was used as the internal standard. The C_3H_8 and CO_2 conversions were defined

as follows:

$$C_3H_8 \text{ conversion}: X_{C_3H_8}(\%) = \frac{F^{in}_{C_3H_8} - F^{out}_{C_3H_8}}{F^{in}_{C_3H_8}} \times 100 \quad (1)$$

$$CO_2 \text{ conversion}: X_{CO_2}(\%) \frac{F^{in}_{CO_2} - F^{out}_{CO_2}}{F^{in}_{CO_2}} \times 100 \quad (2)$$

$$C_3H_6 \text{ sel. in } C_xH_y: S^{C_xH_y}_{C_3H_6}(\%) = \frac{F^{out}_{C_3H_6}}{F^{out}_{C_3H_6} + \frac{2}{3}F^{out}_{C_2H_6} + \frac{2}{3}F^{out}_{C_2H_4} + \frac{1}{3}F^{out}_{CH_4}} \times 100 \quad (3)$$

$$\text{Net } C_3H_6 \text{ sel.}: S^{net}_{C_3H_6}(\%) = \frac{F^{out}_{C_3H_6}}{F^{in}_{C_3H_8} - F^{out}_{C_3H_8}} \times 100 \quad (4)$$

$$\text{CO formed from } CO_2: F^{CO_2}_{CO} = F^{in}_{CO_2} - F^{out}_{CO_2}(\text{ml/min}) \quad (5)$$

$$\text{CO formed from } C_xH_y: F^{C_xH_y}_{CO} = F^{out}_{CO} - F^{CO_2}_{CO}(\text{ml/min}) \quad (6)$$

$$\text{Productivity}: \text{Rate}_{C_3H_6}(\text{mmol}/(g_{cat.}h)) = \frac{F_{C_3H_6} \times 60}{m_{cat.} \times 22.4} \quad (7)$$

$$\text{Carbon balance} = \frac{3F^{out}_{C_3H_8} + 3F^{out}_{C_3H_6} + 2F^{out}_{C_2H_6} + 2F^{out}_{C_2H_4} + F^{out}_{CH_4}}{3F^{out}_{C_3H_8}} \times 100 \quad (8)$$

Where $F^{in}_{C_3H_8}$, $F^{in}_{CO_2}$ and $F^{out}_{C_3H_8}$, $F^{out}_{CO_2}$ mean flow rates of x ($mL{\cdot}min^{-1}$) inlet and outlet the reactor and $m_{cat.}$ means catalyst mass (g). C_3H_8 conversion, CO_2 conversion and C_3H_6 selectivity were distinguished as Eqs. (1–4). Here, CO can be formed from C_xH_y by dry reforming as well as from CO_2 via RWGS reaction, which were distinguished as Eqs. (5) to (6). C_3H_6 reaction formation rate was distinguished as Eq. (7). Carbon balance was distinguished as Eq. (8).

When the catalyst is regenerated, it contains 45 min regeneration at 500 °C under air stream. The flow rate of air is 35 $mL{\cdot}min^{-1}$.

Characterizations

XRD measurements were performed on a Bruker D8 diffractometer operating at 200 mA and 40 kV, employing the graphite filtered Cu **Kα** as the radiation source. The data points were collected by step scanning with a rate of 8°·min^{-1} from 2θ = 10° to 80°.

TEM images were taken using a JEM-2100F transmission electron microscope under a working voltage of 200 kV, equipped with a liquid nitrogen cooled energy dispersive X-ray spectroscopy (EDS) detector for elemental analysis. Aberration-corrected high-angle annular dark-field scanning transmission electron microscopy (AC-HAADF-STEM) images were obtained by JEM-ARM200F, capable of sub-angstrom resolution. The dried catalyst was firstly reduced at 600 °C for 1 h in a stream of 10% H_2/Ar (30 $mL{\cdot}min^{-1}$). Then, the sample powder was dispersed in ethanol by ultrasonic and deposited on a cooper grid coated with an ultrathin holey carbon film.

O_2-TPO. Temperature-programmed oxidation with O_2 was performed on Micromeritics Auto Chem II 2920 chemisorption apparatus equipped with Hiden QIC-20 mass Spectrometer. The 100 mg fresh catalysts that treated 3 h in different reaction atmosphere conditions were pretreated at 300 °C for 1 h under Ar stream, after cooling to 100 °C, 10% O_2 in He (20 $mL{\cdot}min^{-1}$) mixture was switched to reach a stabilized baseline. Finally, the analysis was heated to 800 °C, at a rate of 10 °C·min^{-1}, and the products (CO_2, m/e equal to 44) in the exhaust were measured by the mass spectrometer.

CO_2-TPD. CO_2 temperature-programmed desorption was also performed on the Micromeritics Auto Chem II 2920 chemisorption apparatus. Typically, 100 mg of sample was first treated at 600 °C for 1 h in 10% H_2/Ar (30 $mL{\cdot}min^{-1}$) and then purged with Ar (30 $mL{\cdot}min^{-1}$) for 30 min and cooled down to 50 °C. CO_2 was adsorbed using a flow of 5% CO_2/He (20 $mL{\cdot}min^{-1}$) for 1 h. Finally, the samples were heated to 800 °C at a rate of 10 °C/min under the flow of He (30 $mL{\cdot}min^{-1}$). The output products were measured on Hiden QIC-20 mass spectrometer.

X-ray photoelectron spectroscopy (XPS) was conducted on a Thermo Fisher ESCALAB-Xi equipped with an Al **Kα** X-ray radiation source ($h\nu$ = 1486.6 eV). The binding energies were calibrated using the C1*s* peak at 284.8 eV. Avantage software was used to core-level spectra decomposition. The catalyst was firstly reduced at 600 °C for 1 h in a stream of 10% H_2/Ar (30 $mL{\cdot}min^{-1}$).

H_2-TPR. H_2 temperature-programmed reduction was performed on the Micromeritics Auto Chem II 2920 chemisorption apparatus, 100 mg of sample was treated at 600 °C for 1 h in H_2 atmosphere (30 $mL{\cdot}min^{-1}$) and cooled down to 30 °C in Ar atmosphere (30 $mL{\cdot}min^{-1}$). After that, the sample was flushed with 10% H_2/Ar (20 $mL{\cdot}min^{-1}$) for 5 min and heated at a rate of 10 °C/min up to 800 °C.

H_2-TPD. H_2 temperature-programmed desorption was performed on the Micromeritics Auto Chem II 2920 chemisorption apparatus, 100 mg of sample was treated at 600 °C for 1 h in H_2 atmosphere (30 $mL{\cdot}min^{-1}$), and then the sample was treated at 600 °C for 30 min and cooled down to −10 °C in Ar atmosphere (30 $mL{\cdot}min^{-1}$). Then switch the gas to 10% H_2/Ar for 1 h, after that, the sample was flushed with Ar (20 $mL{\cdot}min^{-1}$) for 30 min and heated at a rate of 10 °C/min up to 800 °C. The MS signals of H_2 (m/e equals to 2) were recorded.

Isothermal and pulse experiments were carried out on the Micromeritics Auto Chem II 2920 chemisorption apparatus, and the output products were also measured on Hiden QIC-20 mass spectrometer). Typically, 100 mg samples were pretreated in U-type reactor at 600 °C for 1 h under 10% H_2/Ar (30 $mL{\cdot}min^{-1}$), after this, the temperature decreased to 500 °C in Ar (30 $mL{\cdot}min^{-1}$). And then, the analysis was carried out using 10 switches back and forth between atmospheres C_3H_8/CO_2/Ar and C_3H_8/Ar for 1 h. The exhausted gas was analysis by online mass spectrometer (CO_2, C_3H_6, C_3H_8, CO, H_2O and H_2, m/e equals to 44, 41, 29, 28, 18 and 2, respectively).

TPSR. Temperature-programmed experiments were all carried out on a fixed-bed reactor equipped with a Mass Spectrometry OmniStar from Pfeiffer Vacuum. For TPSR of C_3H_8 over the fresh catalyst, 100 mg of sample was treated in a flow rate of 35 $mL{\cdot}min^{-1}$ of 40% H_2/Ar at 600 °C for 1 h and cooled down to 50 °C in Ar (35 $mL{\cdot}min^{-1}$). After switching to C_3H_8/Ar (5 $mL{\cdot}min^{-1}$ C_3H_8, 30 $mL{\cdot}min^{-1}$ Ar) for 30 min, the sample was heated at a rate of 10 °C·min^{-1} up to 600 °C. For TPSR of C_3H_8 and CO_2 co-feed over the fresh catalyst, the difference is that switching to C_3H_8/CO_2/Ar (5 $mL{\cdot}min^{-1}$ C_3H_8, 3 $mL{\cdot}min^{-1}$ CO_2, 27 $mL{\cdot}min^{-1}$ Ar) for 30 min. The output products (CO_2, C_3H_6, C_3H_8, CO, H_2O and H_2, m/e equals to 44, 41, 29, 28, 18 and 2, respectively) were monitored by mass spectrometry (MS).

Laser Raman spectroscopy experiments were carried out using a JEOL NRS-5100 spectrometer at 25 °C to investigate the carbonaceous deposits over the spent (3 h) catalysts, with 2 cm^{-1} resolution of the apparatus and a 532 nm excitation source.

In-situ DRIFTS. The In-situ Diffuse Reflectance Infrared Fourier-transform Spectroscopy experiments were carried out on a Nicolet IS50 spectrometer, equipped with a Harrick Scientific DRIFTS cell fitted with ZnSe windows. The detailed treatments are given as the follows:

In-situ DRIFTS experiments were performed to monitor the different of coordination of Pt_1Sn_7/Al_2O_3 and Pt_1Sn_7/CeO_x-Al_2O_3. The fresh catalysts were heated from ambient temperature to 600 °C at a rate of 10 °C·min^{-1} and retained at 600 °C in a flow rate of 35 $mL{\cdot}min^{-1}$ of 40% H_2/

Ar. Then, the catalysts were cooled down to 30 °C and the backgrounds (8 cm^{-1} resolution, 64 scans) were collected after Ar purging in a flow rate of 35 mL·min^{-1} for at least 1 h. With the addition of a flow of 3 mL·min^{-1} of CO, the adsorption of CO molecules on the surface of the catalysts continued for 30 min. After that, the DRIFTS spectra were recorded till no visible change in the absorption band intensities under Ar purging.

In-situ DRIFTS experiments were performed to record the surface species evolution of Pt_1Sn_7/CeO_x-Al_2O_3 during successive treatments with H_2/Ar. The fresh catalyst (50 mg powdered sample) was filled into the reactor. Initially, the fresh catalysts were heated at a rate of 10 °C·min^{-1} from ambient temperature to 500 °C. The systems were then purged with Ar (35 mL·min^{-1}) at 500 °C for 1 h to remove the adsorbates. After that, the background spectra (a resolution of 8 cm^{-1}, 64 scans) were collected. Subsequently, the sample was treated with 40% H_2/Ar (35 mL·min^{-1}) for 1 h, DRIFTS spectra were collected every 1 min. Followed by flushing with Ar (35 mL·min^{-1}) for 10 min.

In-situ DRIFTS experiments were performed to record the surface species evolution of Pt_1Sn_7/CeO_x-Al_2O_3 under reaction conditions (RWGS, PDH, CO_2-PDH). For PDH switch to CO_2-PDH DRIFTS, the fresh catalyst (50 mg powdered sample) was filled into the reactor and flushed with Ar (35 mL·min^{-1}) at 300 °C for 1 h to remove the adsorbates. Then, the catalysts were heated from 300 °C to 600 °C at a rate of 10 °C/min and retained at 600 °C in a flow rate of 35 mL·min^{-1} of 40% H_2/Ar. After this, the catalysts were cooled down to 500 °C and the backgrounds (8 cm^{-1} resolution, 64 scans) were collected after Ar purging in a flow rate of 35 mL·min^{-1} for at least 1 h. the background spectra (a resolution of 8 cm^{-1}, 64 scans) were collected. Afterwards, a C_3H_8/Ar mixture with a flow rate of 35 mL·min^{-1} (5 mL·min^{-1} C_3H_8, 30 mL·min^{-1} Ar) was introduced into the reactor for 32 min, after this, a C_3H_8/CO_2/Ar mixture with a flow rate of 35 mL·min^{-1} (5 mL·min^{-1} C_3H_8, 3 mL·min^{-1} CO_2, 27 mL·min^{-1} Ar) was introduced into the reactor for 58 min. For RWGS, the different is that a H_2/CO_2/Ar mixture with a flow rate of 35 mL·min^{-1} (5 mL·min^{-1} H_2, 5 mL·min^{-1} CO_2, 25 mL·min^{-1} Ar) was introduced into the reactor after pre-reduced. And for CO_2-PDH DRIFTS, the different is that a C_3H_8/CO_2/Ar mixture with a flow rate of 35 mL·min^{-1} (5 mL·min^{-1} C_3H_8, 3 mL·min^{-1} CO_2, 27 mL·min^{-1} Ar) was introduced into the reactor for 32 min directly after pre-reduced. DRIFTS spectra were collected every 1 min.

Data availability

The data generated in this study are provided in Supplementary Information and Source Data file. Data are available from the corresponding authors upon request. Source data are provided with this paper.

References

1. Carter, J. et al. Direct and oxidative dehydrogenation of propane: from catalyst design to industrial application. *Green Chem.* **23**, 9747–9799 (2021).
2. Wang, Y. et al. Color center-rich γ-Al_2O_3 promotes propane dehydrogenation. *Sci. China Chem.* **67**, 4134–4141 (2024).
3. Otroshchenko, T., Jiang, G., Kondratenko, V., Rodemerck, U. & Kondratenko, E. Current status and perspectives in oxidative, non-oxidative and CO_2-mediated dehydrogenation of propane and isobutane over metal oxide catalysts. *Chem. Soc. Rev.* **50**, 473–527 (2021).
4. Wan, H., Gong, N. & Liu, L. Solid catalysts for the dehydrogenation of long-chain alkanes: lessons from the dehydrogenation of light alkanes and homogeneous molecular catalysis. *Sci. China. Chem.* **65**, 2163–2176 (2022).
5. Li, L., Wang, H., Han, J., Zhu, X. & Ge, Q. Balancing the activity and selectivity of propane oxidative dehydrogenation on NiOOH (001) and (010). *Trans. Tianjin Univ.* **26**, 341–351 (2020).
6. Shi, L., Wang, D. & Lu, A.-H. A viewpoint on catalytic origin of boron nitride in oxidative dehydrogenation of light alkanes. *Chin. J. Catal.* **39**, 908–913 (2018).
7. Yan, H. et al. Tandem In_2O_3-Pt/Al_2O_3 catalyst for coupling of propane dehydrogenation to selective H_2 combustion. *Science* **371**, 1257–1260 (2021).
8. Zangeneh, F., Sahebdelfar, S. & Bahmani, M. Propane dehydrogenation over a commercial Pt-Sn/Al_2O_3 catalyst for isobutane dehydrogenation: optimization of reaction conditions. *Chin. J. Chem. Eng.* **21**, 730–735 (2013).
9. Sun, G. et al. Metastable gallium hydride mediates propane dehydrogenation on H_2 co-feeding. *Nat. Chem.* **16**, 575–583 (2024).
10. Gomez, E., Yan, B., Kattel, S. & Chen, J. G. Carbon dioxide reduction in tandem with light-alkane dehydrogenation. *Nat. Rev. Chem.* **3**, 638–649 (2019).
11. Ansari, M. & Park, S.-E. Carbon dioxide utilization as a soft oxidant and promoter in catalysis. *Energy Environ. Sci.* **5**, 9419–9437 (2012).
12. Rigamonti, M., Shah, M., Gambu, T., Saeys, M. & Dusselier, M. Reshaping the role of CO_2 in propane dehydrogenation: from waste gas to platform chemical. *ACS Catal.* **12**, 9339–9358 (2022).
13. Gomez, E. et al. Combining CO_2 reduction with propane oxidative dehydrogenation over bimetallic catalysts. *Nat. Commun.* **9**, 1398 (2018).
14. Xie, Y., Hua, W., Yue, Y. & Gao, Z. Dehydrogenation of propane to propylene over Ga_2O_3 supported on mesoporous HZSM-5 in the presence of CO_2. *Chin. J. Chem.* **28**, 1559–1564 (2010).
15. Dou, J. et al. $Ce_xZr_{1-x}O_2$-supported CrO_x catalysts for CO_2-assisted oxidative dehydrogenation of propane-probing the active sites and strategies for enhanced stability. *ACS Catal.* **13**, 213–223 (2023).
16. Liu, Y. et al. Promoting propane dehydrogenation with CO_2 over Ga_2O_3/SiO_2 by eliminating Ga-hydrides. *Chin. J. Catal.* **42**, 2225–2233 (2021).
17. Yang, G.-Q. et al. Promotional nature of Sn on Pt/CeO_2 for the oxidative dehydrogenation of propane with carbon dioxide. *Nano Res.* **16**, 6237–6250 (2023).
18. Xing, F., Nakaya, Y., Yasumura, S., Shimizu, K.-i & Furukawa, S. Ternary platinum-cobalt-indium nanoalloy on ceria as a highly efficient catalyst for the oxidative dehydrogenation of propane using CO_2. *Nat. Catal.* **5**, 55–65 (2022).
19. Zhai, P. et al. CO_2-mediated oxidative dehydrogenation of propane enabled by Pt-based bimetallic catalysts. *Chem* **9**, 3268–3285 (2023).
20. Yan, B. et al. Active sites for tandem reactions of CO_2 reduction and ethane dehydrogenation. *Proc. Natl. Acad. Sci. U.S.A.* **115**, 8278–8283 (2018).
21. Kim, H., Gu, J., Byun, M., Choe, C. & Lim, H. Novel propane dehydrogenation process design integrated with membrane reactor and solid oxide fuel cell: economic and environmental aspects. *J. Environ. Chem. Eng.* **11**, 110830 (2023).
22. Xiang, D., Li, P. & Xia, Y. Conceptual design and techno-economic analysis of a novel propane dehydrogenation process integrated with chemical looping combustion and CO_2 hydrogenation. *Energ. Convers. Manage.* **281**, 116820 (2023).
23. Garg, S., Xie, Z. & Chen, J. G. Tandem reactors and reactions for CO_2 conversion. *Nat. Chem. Eng.* **1**, 139–148 (2024).
24. Pei, C., Chen, S., Fu, D., Zhao, Z.-J. & Gong, J. Structured catalysts and catalytic processes: transport and reaction perspectives. *Chem. Rev.* **124**, 2955–3012 (2024).
25. Qin, J. et al. Techno-economic analysis of a hybrid process for propylene and ammonia production. *ACS Sustain. Chem. Eng.* **10**, 6999–7009 (2022).
26. Wei, X. et al. Bimetallic clusters confined inside silicalite-1 for stable propane dehydrogenation. *Nano Res.* **16**, 10881–10889 (2023).
27. Motagamwala, A., Almallahi, R., Wortman, J., Igenegbai, V. & Linic, S. Stable and selective catalysts for propane dehydrogenation operating at thermodynamic limit. *Science* **373**, 217–222 (2021).
28. Zhuang, G., Chen, Y., Zhuang, Z., Yu, Y. & Yu, J. Oxygen vacancies in metal oxides: recent progress towards advanced catalyst design. *Sci. China Mater.* **63**, 2089–2118 (2020).

29. Wang, W. et al. Tandem propane dehydrogenation and surface oxidation catalysts for selective propylene synthesis. *Science* **381**, 886–890 (2023).
30. Wang, H. et al. Integrating ceria with cobalt sulfide as high-performance electrocatalysts for overall water splitting. *Fundam. Res.* **3**, 356–361 (2023).
31. Campbell, C. & Peden C. Oxygen vacancies and catalysis on ceria surfaces. *Science* **309**, 713–714 (2005).
32. ung, J.-W., Kim, W.-I., Kim, J.-R., Oh, K. & Koh, H. Effect of direct reduction treatment on Pt-Sn/Al_2O_3 catalyst for propane dehydrogenation. *Catalysts* **9**, 446 (2019).
33. Xing, Y. et al. Sn_1Pt single-atom alloy evolved stable PtSn/nano-Al_2O_3 catalyst for propane dehydrogenation. *Chin. J. Catal.* **48**, 164–174 (2023).
34. Alvarez, A. et al. CO_2 activation over catalytic surfaces. *Chem. Phys. Chem.* **18**, 3135–3141 (2017).
35. Cheng, Z., Sherman, B. & Lo, C. Carbon dioxide activation and dissociation on ceria (110): a density functional theory study. *J. Chem. Phys.* **138**, 014702 (2013).
36. Weisz, P. & Swegler, E. Stepwise reaction on separate catalytic centers: isomerization of saturated hydrocarbons. *Science* **126**, 31–32 (1957).
37. Wang, Q., Tichit, D., Meunier, F. & Guesmi, H. Combined DRIFTS and DFT study of CO adsorption and segregation modes in Pt-Sn nanoalloys. *J. Phys. Chem. C* **124**, 9979–9989 (2020).
38. Lee, J. & Christopher, P. Does H_2 temperature-programmed reduction always probe solid-state redox chemistry? The case of Pt/CeO_2. *Angew. Chem. Int. Edit.* **64**, e202414388 (2025).
39. Conner, W. C. Jr. & John, L. F. Spillover in heterogeneous catalysis. *Chem. Rev.* **95**, 759–788 (1995).
40. Kurniawan, R. G. et al. Direct conversion of furfural to 1,5-pentanediol over a nickel-cobalt oxide-alumina trimetallic catalyst. *Appl. Catal. B: Environ.* **320**, 121971 (2023).
41. Cao, C. et al. Selective hydrogenolysis of furfuryl alcohol towards 1,5-pentanediol over a Co/CeO_2 catalyst. *Catal. Sci. Technol.* **15**, 2928–2937 (2025).
42. Zhang, L. L., Ren, Y. J., Liu, W. G., Wang, A. Q. & Zhang, T. Single-atom catalyst: A rising star for green synthesis of fine chemicals. *Natl. Sci. Rev.* **5**, 653–672 (2018).
43. Wu, W., Savereide, L., Notestein, J. & Weitz, E. In-situ IR spectroscopy as a probe of oxidation/reduction of Ce in nanostructured CeO_2. *Appl. Surf. Sci.* **445**, 548–554 (2018).
44. Werner, K. et al. Toward an understanding of selective alkyne hydrogenation on ceria: on the impact of O vacancies on H_2 interaction with CeO_2 (111). *J. Am. Chem. Soc.* **139**, 17608–17616 (2017).
45. Zhang, W., Pu, M. & Lei, M. Theoretical studies on the stability and reactivity of the metal-doped CeO_2 (100) surface: toward H_2 dissociation and oxygen vacancy formation. *Langmuir* **36**, 5891–5901 (2020).
46. Parastaev, A. et al. Boosting CO_2 hydrogenation via size-dependent metal-support interactions in cobalt/ceria-based catalysts. *Nat. Catal.* **3**, 526–533 (2020).
47. Karim, W. et al. Catalyst support effects on hydrogen spillover. *Nature* **541**, 68–71 (2017).
48. Alayoglu, S. et al. Pt-mediated reversible reduction and expansion of CeO_2 in Pt nanoparticle/mesoporous CeO_2 catalyst: in situ X-ray spectroscopy and diffraction studies under redox (H_2 and O_2) atmospheres. *J. Phys. Chem. C* **117**, 26608–26616 (2013).
49. Lykhach, Y. et al. Hydrogen spillover monitored by resonant photoemission spectroscopy. *J. Catal.* **285**, 6–9 (2012).
50. Lee, J. et al. How Pt influences H_2 reactions on high surface-area Pt/CeO_2 powder catalyst surfaces. *JACS Au* **3**, 2299–2313 (2023).
51. Kolyagin, Y. et al. Initial stages of propane activation over Zn/MFI catalyst studied by in situ NMR and IR spectroscopic techniques. *J. Catal.* **238**, 122–133 (2006).
52. Ye, C. et al. Atomically dispersed Pt in ordered PtSnZn intermetallic with Pt-Sn and Pt-Zn pairs for selective propane dehydrogenation. *Sci. China Mater.* **66**, 1071–1078 (2023).
53. Zhou, J. et al. Enhanced performance for propane dehydrogenation through Pt clusters alloying with copper in zeolite. *Nano Res.* **16**, 6537–6543 (2023).
54. Jones, J. et al. Thermally stable single-atom platinum-on-ceria catalysts via atom trapping. *Science* **353**, 150–154 (2016).
55. Hu, J., Li, Y., Zhen, Y., Chen, M. & Wan, H. In situ FTIR and ex situ XPS/HS-LEIS study of supported Cu/Al_2O_3 and Cu/ZnO catalysts for CO_2 hydrogenation. *Chin. J. Catal.* **42**, 367–375 (2021).
56. Shen, H. et al. Identifying the roles of Ce^{3+}-OH and Ce-H in the reverse water-gas shift reaction over highly active Ni-doped CeO_2 catalyst. *Nano Res.* **15**, 5831–5841 (2022).
57. Zhu, M., Ge, Q. & Zhu, X. Catalytic reduction of CO_2 to CO via reverse water gas shift reaction: recent advances in the design of active and selective supported metal catalysts. *Trans. Tianjin Univ.* **26**, 172–187 (2020).
58. Wang, W., Qu, Z., Song, L. & Fu, Q. CO_2 hydrogenation to methanol over Cu/CeO_2 and Cu/ZrO_2 catalysts: tuning methanol selectivity via metal-support interaction. *J. Energy Chem.* **40**, 22–30 (2020).
59. Mansour, H. & Iglesia, E. Mechanistic connections between CO_2 and CO hydrogenation on dispersed ruthenium nanoparticles. *J. Am. Chem. Soc.* **143**, 11582–11594 (2021).
60. Sun, J. et al. Role of oxygen transfer and surface reaction in catalytic performance of VO_x-$Ce_{1-x}Zr_xO_2$ for propane dehydrogenation. *Chin. J. Catal.* **52**, 217–227 (2023).
61. Zhang, W. et al. Size dependence of Pt catalysts for propane dehydrogenation: from atomically dispersed to nanoparticles. *ACS Catal.* **10**, 12932–12942 (2020).
62. Zhu, J. et al. Size-dependent reaction mechanism and kinetics for propane dehydrogenation over Pt catalysts. *ACS Catal.* **5**, 6310–6319 (2015).
63. Kwan, E., Park, Y., Besser, H., Anderson, T. & Jacobsen, E. Sensitive and accurate ^{13}C kinetic isotope effect measurements enabled by polarization transfer. *J. Am. Chem. Soc.* **139**, 43–46 (2017).
64. Biswas, A., Xie, Z. & Chen, J. G. Can CO_2-assisted alkane dehydrogenation lead to negative CO_2 emissions? *Joule* **6**, 269–273 (2022).
65. Zhang, F., Miao, C., Yue, Y., Hua, W. & Gao, Z. Dehydrogenation of propane to propylene in the presence of CO_2 over steaming-treated HZSM-5 supported ZnO. *Chin. J. Chem.* **30**, 929–934 (2012).
66. Xie, S. et al. Pt atomic single-layer catalyst embedded in defect-enriched ceria for efficient CO oxidation. *J. Am. Chem. Soc.* **144**, 21255–21266 (2022).

Acknowledgements

This work is financially supported by the National Key R&D Program of China (2023YFA1507800), the National Science Foundation of China (No. 22121004, 22122808, 22478279, and 22108201), the Haihe Laboratory of Sustainable Chemical Transformations, the Program of Introducing Talents of Discipline to Universities (BP0618007), and the XPLORER PRIZE.

Author contributions

J.L.G. and C.L.P. initiated and supervised the research. K.G.T. performed the catalyst preparation. K.G.T., S.C., and G.D.S. designed and performed the catalytic reaction and kinetic test. K.G.T., S.C., D.L.F., and X.H.W. performed the characterization. J.H.C. and Z.Y.W. performed the CO_2 footprint analysis. K.G.T., S.C., Z.-J.Z., D.L.F., C.L.P. and J.L.G. analyzed the data and wrote the paper. All authors contributed to the

discussion of the research and approved the final version of the manuscript.

Competing interests
The authors declare no competing interests.

Additional information
Supplementary information The online version contains supplementary material available at https://doi.org/10.1038/s41467-025-65261-6.

Correspondence and requests for materials should be addressed to Chunlei Pei or Jinlong Gong.

Peer review information *Nature Communications* thanks Michiel Dusselier, and the other anonymous, reviewer(s) for their contribution to the peer review of this work. A peer review file is available.